

Attribution-NonCommercial-NoDerivatives 4.0 International (CC BY-NC-ND 4.0)  
<https://creativecommons.org/licenses/by-nc-nd/4.0/>

Access to this work was provided by the University of Maryland, Baltimore County (UMBC) ScholarWorks@UMBC digital repository on the Maryland Shared Open Access (MD-SOAR) platform.

**Please provide feedback**

Please support the ScholarWorks@UMBC repository by emailing [scholarworks-group@umbc.edu](mailto:scholarworks-group@umbc.edu) and telling us what having access to this work means to you and why it's important to you. Thank you.

**Incorporating vascular-stasis based blood perfusion to evaluate the thermal signatures of cell-death using modified Arrhenius equation with regeneration of living tissues during nanoparticle-assisted thermal therapy**

Manpreet Singh

Department of Mechanical Engineering,  
University of Maryland Baltimore County,  
Baltimore, MD, USA

**\*Correspondence**

Manpreet Singh, Ph.D. (P), M.E., B-Tech  
Department of Mechanical Engineering,  
College of Engineering and Information Technology,  
University of Maryland Baltimore County,  
1000 Hilltop Circle, Baltimore, MD-21250, United States.  
Phone: +1 (667)900-2626; Email: [snamra.manpreet@gmail.com](mailto:snamra.manpreet@gmail.com)

**Journal:** *International Communications in Heat and Mass Transfer.*

**Cover Title:** *Implementing Non-Arrhenius kinetics in nanoparticle assisted thermal therapy.*

## ABSTRACT

Cellular and biological tissue heating may result in reversible (or repairable injury) and irreversible (or lethal) thermal cell-death in living biological tissues. Continuous regeneration of living human tissues due to the continuous supply of oxygen through arterial blood must be taken into account to counter balance the thermal degradation at quasi-static thermal conditions. This study incorporates vascular-stasis based non-linear blood perfusion for magnetic nanoparticle assisted thermal therapy to model the *thermal bystander effect* - a hyperthermia-induced deep infiltration of nanoparticles in the targeted tissue domain. Pennes bioheat model based on Fourier heat conduction theory is four-way coupled with Arrhenius and non-Arrhenius kinetic models of cell-death with healthy cells regeneration. In determination of treatment endpoint, the kinetic model must be coupled with quantitative and qualitative pathological biomarkers of thermal damage. Nanoparticle distribution volume increases by 39.62% after possible rupturing of cell membrane during heating. The release of intracellular solution by dead cells during heating promotes nanoparticle migration from the region of higher concentration to the regions of lower concentration thereby 80% enhancement in interstitial space and five-fold increase in diffusion coefficient. For such redistribution phenomenon, the heating time is sufficient to reduce the oxygen in erythrocytes (red blood cells) and maximize the necrosis zone inside tumour. However, at the interface, the regeneration of healthy cells triggers an immune response of biological tissue towards continued heating to suppress, prevent and restrict further accumulation of thermal damage within damage bounds of  $\Omega \leq 1$ . While modelling the kinetics of thermal damage of tumour, one must include and should not ignore the partial self-regeneration of connecting normal human tissues at the tumour periphery due to continuous matching of oxygen demands in the healthy tissue by the arterial blood.

**Keywords:** Modified thermal cell-death model; Healthy cells regeneration; Vascular-Stasis based blood perfusion, Nanoparticles assisted heating; Heterogeneous distribution and redistribution of nanoparticles; Cell-necrosis induced porosity and diffusion enhancement; Cancer; Bioheat transfer.

## Nomenclature

$A$	pre-exponential or frequency factor, (s <sup>-1</sup> )
$b$	Wien's constant
$B$	regeneration coefficient
$c_p$	specific heat capacity, (J/kg °C)
$c$	speed of light in vacuum
$C$	volume-averaged nanoparticle concentration, (mol/m <sup>3</sup> )
$D_n$	diffusion coefficient, (m <sup>2</sup> /s)
$D_{n,f}$	nanoparticle diffusion coefficient in unbound interstitial fluid, (m <sup>2</sup> /s)
$E_a$	activation energy, (J/mol)
$E_o$	total energy emitted per unit surface area of a black body
$g$	acceleration due to gravity
$\bar{h}$	convective heat transfer coefficient, (W/m <sup>2</sup> °C)
$k_B$	Boltzmann constant
$k$	thermal conductivity, (W/m °C)
$Pr$	Prandtl number
$q_{ck}$	sum of the heat flow density between the object-thermography equipment, (W/m <sup>2</sup> )
$Q'''_{met}$	volumetric heat generation rate due to metabolism, (W/m <sup>3</sup> )
$Q'''_{source}$	heterogeneously-distributed volumetric heat source contribution by nanoparticles, (W/m <sup>3</sup> )
$R_u$	universal gas constant (J/mol °C)
$t$	time, (s)
$T$	absolute temperature, (°C)
$x$	position coordinate in the $x$ -direction
$y$	position coordinate in the $y$ -direction
$z$	position coordinate in the $z$ -direction
$\nabla$	laplacian differential operator

## Abbreviations

$HU$	hounsfield units
$GS$	grayscale
$PC3$	human prostate cancer cell line
$MUMPS$	multifrontal massively parallel sparse
$microCT$	microcomputed tomography
$PBHTE$	pennes bioheat transfer equation
$MNATT$	magnetic nanoparticle assisted thermal therapy
$CNIDC$	cell necrosis induced diffusivity change
$CNIPE$	cell necrosis induced porosity enhancement
$MNPs$	magnetic nanoparticles

$SAR$	specific absorption rate
$FEA$	finite element analysis

## Greek symbols

$\alpha$	thermal diffusivity (m <sup>2</sup> /s)
$\hbar$	Planck's constant, (-)
$\rho$	density, (kg/m <sup>3</sup> )
$\sigma$	Stefan Boltzmann's constant, (-)
$\Omega$	induced thermal damage, (-)
$\omega_b$	blood perfusion rate, (s <sup>-1</sup> )
$\lambda$	wavelength of emission, (1/m)
$\theta$	degree of vascular stasis, (-)
$\phi$	interstitial volume fraction or porosity, (-)
$\tau$	any time instant (s)
$\varepsilon$	radiative property of the surface termed as emissivity, (-)
$\zeta$	Concentration of tissue constituent
$\xi$	an index to evaluate vascular stasis using arrhenius equation
$\nu$	kinematic viscosity (m <sup>2</sup> /s)
$\beta$	volume coefficient of air expansion evaluated at mean value of surface and air temperature (1/K)

## Subscripts

$b$	arterial/blood
$0$	initial value or before heating
$mouse$	mouse body region
$tumor$	implanted PC3 tumor region
$met$	metabolic
$amb$	ambient conditions
$bs$	bulk skin
$perf$	perfusion
$min$	minimum
$avg$	average
$max$	maximum
$h$	healthy tissue
$c$	cancerous tissue
$mir$	mirrored
$air$	referred to air
$conv$	convective
$rad$	radiation
$lumped$	equivalent of radiation and convection
$f$	film

## 1. Introduction

The thermal damage predictions by first-order Arrhenius kinetic rate equation gives us monotonic degradation of living tissues along with cancerous lesions [**Dombrovsky, 2022**]. For low temperature hyperthermia ( $T \leq 41^\circ\text{C}$ ) i.e. at diathermic temperatures, biological tissues shows an accelerated tissue recovery and repair with an evident rise in blood perfusion levels and associated metabolic demands. At the temperature range of  $40\text{--}42^\circ\text{C}$ , some transformations and molecular-level changes in tumour cells might have been already initiated.

Tissue regeneration mechanisms during burn injury remains unclarified. Healthy cells regeneration and thermal ablation are occurring concurrently in living cells and such mechanisms were not properly addressed in the context of burn injury. One hypothesis suggests the possibility of continuous regeneration of living human tissues due to continuous meeting of oxygen demands supplied by erythrocytes of the arterial blood [**Dombrovsky and Timchenko, 2015**]. Hence, due to this regeneration process, the biological tissues shows an accelerated tissue repair and recovery with an evident rise in blood perfusion levels. Previous studies by research groups [**Kumar and Rai, 2016; Liu and Chen, 2021**] implemented regeneration term into Arrhenius formulation; however, effect of hyperemic region through vascular stasis (non-linear perfusion change) [implemented in **Prakash et al., 2012** and adapted from **Schutt and Haemmerich, 2008**] is missing for such regeneration based model. **Alzahrani and Abbas, 2019** employed an analytical approach associated with Laplace transformation, experimental temperature, and a sequential concept over time to obtain the thermal damage and the temperature in a living tissue. **Kabiri and Talaee, 2019** and **Talaee and Kabiri, 2017** analyzed hyperbolic behavior of non-Fourier bioheat equation over parabolic Fourier bioheat equation to estimate temperature profiles in cylindrical and spherical coordinate system respectively using Eigen value method to improve the reliability of clinical protocols.

In the discussions pertinent to tissue regeneration and tissue repair, it has been shown that several parenchymal cells and tissues holds capabilities to regenerate themselves after necrosis. It has been explicitly stated by **Thomsen and Pearce, 2010** that irrespective of the employed tissue injury mechanism (laser, electromagnetic, microwave or radiofrequency ablation etc.), squamous metaplasia can be frequently seen in regenerated tissues of solid glandular structures such as prostate and breast tissues respectively and as well as epidermis of the skin, liver cells, glandular epithelium of gastrointestinal tract. As long as the normal tissue connective architecture remain intact, the regenerating cells will be guided towards connective tissue scaffolding to form normal functional tissue structures. The available precursor cells (stem cells) in the surrounding viable tissues can migrate, proliferate and mature in response to numerous growth factors produced by the residual, living connective tissue and inflammatory cells at the periphery of cancerous lesion. It would also be true to state that if there is large volume necrosis, large

volume parenchymal cell generation may not occur at all and tissue repair would mainly be due to the prominence of fibrous scar tissue formation relative to glandular epithelial regeneration for pig breasts. The regenerating new epithelial cells may have changed (metaplasia) from low columnar ductal epithelial cells to larger, more deeply staining stratified squamous epithelial cells [Thomsen and Pearce, 2010].

MicroCT imaging assisted *in-vitro* agarose gel studies and *in-vivo* animal studies have suggested possible change in nanoparticle distribution after heating [Gu et al., 2017; Gu et al., 2019; Singh et al., 2019; Singh et al., 2020]. According to one study, the nanoparticles distribution becomes more homogeneous in regions of necrosis [Johannsen et al., 2004]. Another study demonstrates that heating may cause 2.5 fold enhancement in the intratumoural iron concentration [Jordan et al., 1997]. Miaskowski and Subramanian, 2019 demonstrate that immobilized state of magnetic nanoparticles within the tumour volume results in 30% decrease in heat dissipation rates as compared to mobilized or redistributed state of nanoparticles. The experiments performed by Gu et al., 2019 suggests that magnetic nanoparticle distribution volume was 95% larger in the heating group for low heat generation rates while 10% smaller in the heating group for high heat generation rates. The redistribution of nanoparticles from the region of higher concentration to the region of lower concentration is described as “Thermal By-Stander Effect”- which is a hyperthermia induced deep infiltration of nanoparticles event taking place in the targeted tissue domain [Attaluri et al., 2015]. This underdeveloped issue is also quantified in present simulation framework that heating induce migration of nanoparticles, governs the spatiotemporal temperature profile during regeneration of healthy cells.

This study aims to investigate four issues: (1) the implications of incorporating regeneration of healthy tissues into Arrhenius formulation for magnetic nanoparticle assisted thermal therapy (MNATT), (2) To study the effect of hyperemic region through vascular stasis (fractional injury) based non-linear microvascular perfusion change, and (3) To answer reasons behind magnetic nanoparticles migration, (4) Extent of redistribution of nanoparticles following heating for such regeneration based model.

## 2. Material and methods

### 2.1. Assessment of skin surface temperatures using infrared thermo-imaging

Heat transfer in biological tissues is mainly due to three underlying physical mechanisms: thermal conduction, thermal convection and thermal radiation. Infrared thermo-imaging works on the principle of thermal radiation (wavelengths varying between threshold window of 760 nm – 1 mm). This window of wavelength range is further classified as near infrared (760 nm – 2.5  $\mu$ m), middle infrared (2.5 – 50  $\mu$ m) and far infrared (50  $\mu$ m – 1 mm). In this study, infrared imaging is employed to extract realistic physiological parameters (blood perfusion, metabolic heat generation rates) from the information of acquired surface

temperature through inverse heat transfer. Indirect measurement of these physiological parameters is obtained by applying an initial guess to unknown parameters to match thermo-imaging temperatures.

Wien's law and Stefan-Boltzmann's law are employed that takes into account the infrared radiation emitted from the biological tissue or object under consideration, radiation of the environment (background) and radiation of the atmosphere. The Wien's law states that the radiation power maximum emitted by black body is inversely proportional to the thermodynamic temperature i.e.

$$\lambda_{max} = \frac{b}{T} \quad (1)$$

where,  $\lambda_{max}$  is the wavelength of maximum emission,  $T$  is the body temperature,  $b$  is called Wien's constant ( $b = 2.89878 \times 10^{-3}$  mK). The Stefan-Boltzmann law states that the total energy,  $E_o$  emitted per unit surface area of a black body is directly proportional to the fourth power of the black body thermodynamic temperature  $T$  i.e.

$$E_o = \sigma \cdot T^4 \quad (2)$$

where,  $\sigma$  is the Stefan Boltzmann's constant which can be derived from other physical constants as;

$$\sigma = \frac{2\pi^5 k_B^4}{15c^2 \hbar^3} \quad (3)$$

where,  $k_B$  is the Boltzmann constant,  $\hbar$  is Planck's constant, and  $c$  is speed of light in vacuum. A body that does not absorb all incident radiation (grey body:  $\varepsilon < 1$ ) emits less energy than a black body ( $\varepsilon = 1$ ) and is stated as;

$$E = \varepsilon \cdot \sigma \cdot T^4 \quad (4)$$

The computational thermal model consisted of a PC3 tumour (approximately 10 - 12 mm experimental size as measurable by vernier calliper) implanted on the same flank position of the mouse body is adapted from our previous work [Singh et al., 2021b]. The thermal image acquisition is performed through an infrared camera (Fluke TIS45, Fluke Corporation, Everett, WA) to evaluate the temperature uncertainty associated with an unknown skin surface emissivity of Balb/c Nu/Nu male mouse skin and implanted irregular PC3 tumour. The skin surface temperature acquisition requires inputs of both the emissivity and the environmental temperature. It has been shown that normal skin emissivity varies from 0.95 to 0.99, depending on the skin complexion/tone. Theoretical principles of infrared thermography can be employed to predict the surface temperature based on emissivity and ambient temperature as model inputs [Bernard et al., 2013].

$$T = \sqrt[4]{\frac{\frac{q_{ck}}{\sigma} + T_{amb}^4 - (1 - \varepsilon) \cdot T_{mir}^4}{\varepsilon}} \quad (5)$$

Following the work of **Li et al., 2016**, this aforementioned relationship is slightly modified to estimate the thermal imaging temperature

$$T = \sqrt[4]{\frac{q_{ck}}{\sigma\varepsilon} + \frac{(1-\varepsilon)}{\varepsilon} \cdot T_{amb}^4} \quad (6)$$

where,  $T_{amb}$  is the ambient temperature of environment and thermocamera,  $T_{mir}$  is the mirrored temperature of other object which is in optical contact with analysed object or geometrical entity under consideration,  $q_{ck}$  is the sum of the heat flow density between the object and thermography equipment,  $\sigma$  is the Stefan Boltzmann's constant ( $\sigma = 5.67 \times 10^{-8} \text{ W/m}^2 \cdot \text{K}^4$ ),  $\varepsilon$  is the emissivity of the surface or region of interest. The acquired infrared images shows maximum, minimum, and average temperatures respectively for mouse body and tumour region respectively. Mouse is assumed as near cylindrical and PC3 tumour as near spherical. It is to note that it is not always possible to match all three temperature distribution for both domains due to several associated uncertainties. Overall lumped heat transfer coefficient is extracted using empirical correlations as recommended for simpler geometries as;

$$\bar{h}_{lumped} = \bar{h}_{conv} + \bar{h}_{rad} \quad (7)$$

$$\text{where, } \bar{h}_{rad} = \varepsilon\sigma(T_s + T_\infty)(T_s^2 + T_\infty^2) \quad (8)$$

$$\bar{h}_{tumour,conv} = \frac{\left[ 2 + \frac{0.589 \left[ \frac{g\beta(T_{s,tumour} - T_\infty)D_{tumour}^3}{v\alpha} \right]^{1/4}}{[1 + (0.469/Pr)^{9/16}]^{4/9}} \right] k_{air}}{D_{tumour}} \quad (9)$$

$$\bar{h}_{mouse,conv} = \frac{\left[ 0.60 + \frac{0.387 \left[ \frac{g\beta(T_{s,mouse} - T_\infty)D_{mouse}^3}{v\alpha} \right]^{1/16}}{[1 + (0.559/Pr)^{9/16}]^{8/27}} \right] k_{air}}{D_{mouse}} \quad (10)$$

where,  $g$  is the local acceleration due to gravity ( $\text{m/s}^2$ ),  $\beta$  is the volume coefficient of air expansion evaluated at mean value of surface and air temperature ( $1/\text{K}$ ),  $v$  is the kinematic viscosity ( $\text{m}^2/\text{s}$ ),  $\alpha$  is the thermal diffusivity ( $\text{m}^2/\text{s}$ ),  $k_{air}$  is the thermal conductivity of air respectively,  $\varepsilon$  is the radiative property of the surface termed as emissivity,  $D_{tumour}$  (extracted information of  $x,y,z$  coordinates) and  $D_{mouse}$  (equivalent to experimentally extracted mouse body i.e. 0.035 m) are the average diameters of PC3 tumour and mouse respectively. The volume of PC3 tumour is computed as 1014.8  $\text{mm}^3$ . It is to remark that all properties are evaluated at the film temperature,  $T_f \equiv (T_s + T_\infty)/2$ , Prandtl no.,  $Pr = 0.707$ . This effective lumped heat transfer coefficient is used to extract blood perfusion values and mapping of the infrared imaging results



with the theoretical simulations. However, we are able to obtain a close resemblance with the average temperature of both PC3 tumour region and region of interest (circular region) on mouse body (12 mm in diameter) after performing iterative simulations. Additional details regarding its implementation can be referred from our forthcoming work under review [Singh et al., 2022].

## 2.2. Mathematical Model

Let  $\psi \subset \mathbb{R}^3$  be the tumour geometry which is obtained after segmentation and image processing of MicroCT images using SAS® program and MATLAB® program. The boundary of tumour exposed to ambient environment is defined as  $\Gamma$ . The contact zone between tumour and healthy tissue is represented as an interface of two tissues. Let  $T(x,y,z,t)$  be the tissue temperature at positional coordinates  $x,y,z \in \psi$  and time  $t \in [0, t_{end}]$ . This parameter is coupled with other multiphysics variables. Micro-CT cross-sectional slices containing three-dimensional cluster of pixels corresponds to magnetic nanoparticles are converted into volumetric heat generation rate and imported into Comsol-Multiphysics finite element analysis (FEA) platform as an import map. Geometrical description and wireframe model is shown in **fig. 1**.

### 2.2.1. Thermal modeling using Pennes Bioheat Equation: Temperature computation

The classical Fourier's law based Pennes Bioheat Transfer Equation (PBHTE) [Pennes, 1948] is a heat accumulation model that is used to compute the temperature field distribution in both the healthy tissue and cancerous tissue domain as per equations (11a) and (11b) respectively. It was assumed that the arterial blood temperature,  $T_b$  is uniform throughout the biological tissue while the venous blood temperature is equal to the temperature of local tissue ( $T_h$  or  $T_c$ ).

$$\rho_h c_{p,h} \frac{\partial T_h}{\partial t} = k_h \nabla^2 T_h + \omega_{h,0} \rho_b c_{p,b} (T_b - T_h) + Q'''_{met,h} \quad (11a)$$

$$\rho_c c_{p,c} \frac{\partial T_c}{\partial t} = k_c \nabla^2 T_c + \omega_{c,0} \rho_b c_{p,b} (T_b - T_c) + Q'''_{met,c} + Q'''_{source} \quad (11b)$$

Here, the subscripts,  $h$  and  $c$  represents healthy and cancerous tissue domains respectively. Also,  $met$  represents metabolic,  $b$  represents blood and  $source$ , is the heat source contribution (Specific Absorption Rate-SAR) of heterogeneously distributed magnetic nanoparticles when subjected to alternating magnetic field [LeBrun et al., 2016a; Gu et al., 2019]. Pixel numbers or grayscale values (pixel intensities range from 0 being black to 255 being white) from microCT images are converted into Hounsfield Units (HU) to quantify volumetric heat generation rate at each spatial location.

$$Q'''_{source} \left( \frac{W}{m^3} \right) = \begin{cases} 0, & HU \leq HU_{threshold} \\ q'''_{specimen} \frac{HU - HU_{tissue(threshold)}}{HU_{ferrofluid \text{ at } 5.8\%} - HU_{tissue(threshold)}}, & HU > HU_{threshold} \end{cases} \quad (12)$$

where,  $q'''_{\text{specimen}} = 3.4 \times 10^6 \text{ W/m}^3$ ;  $\text{HU} = -1000 \times \frac{\text{GS} - \text{GS}_{\text{water}}}{\text{GS}_{\text{air}} - \text{GS}_{\text{water}}}$ ;  $\text{HU}_{\text{air}} = -1000$ ;  $\text{HU}_{\text{ferrofluid at 5.8\%}} = 2750$ ;  $\text{HU}_{\text{water}} = 0$ ;  $\text{HU}_{\text{threshold}} = \text{without nanoparticles}$ . Based on 5.8% concentration of magnetic nanoparticles, the volumetric heat generation term is expressed into volumetric concentration source map that is imported as an initial condition to Concentration equation. The volumetric heat generation rate,  $Q'''_{\text{source}} \left( \frac{\text{W}}{\text{m}^3} \right)$  is coupled to the volume-averaged nanoparticle concentration in the tissue (mol per unit volume of tissue),  $C(x, y, z, t)$  [Singh et al., 2021b] which is updated at each time step with the progression of time.

$$Q'''_{\text{source}} \left( \frac{\text{W}}{\text{m}^3} \right) = 2266.67 \times C(x, y, z, t) \quad (13)$$

### 2.2.2. Nanoparticle diffusion: Concentration computation

The governing differential equation for nanoparticle diffusion in a porous medium [Truskey, 2009; Singh et al., 2019a] is given as;

$$\frac{\partial C(x, y, z, t)}{\partial t} = \nabla \cdot \left[ \phi D_n \nabla \left( \frac{C(x, y, z, t)}{\phi} \right) \right] \quad (14)$$

where, the diffusion coefficient ( $D_n$ ) relates to interstitial space ( $\phi$ ) and diffusion coefficient in unbound interstitial fluid ( $D_{n,f}$ ) [Zhang et al., 2009; El-Kareh et al., 1993] as;

$$D_n = D_{n,f} \left[ \frac{2\phi}{3 - \phi} \right] \quad (15)$$

**Table-I:** Thermophysical properties [Singh et al., 2021b; Kumar and Rai, 2016].

Property	Symbol [Units]	Healthy Tissue	Cancerous Tissue	Blood
Thermal conductivity	$k$ [W/(mK)]	0.5	0.5	0.55
Density	$\rho$ [kg/m <sup>3</sup> ]	1060	1060	1060
Specific heat capacity	$c_p$ [J/(kgK)]	3780	3780	3780
Baseline blood perfusion	$\omega_b$ [m <sup>3</sup> /(sm <sup>3</sup> )]	0.00285 <sup>#</sup>	0.00111 <sup>#</sup>	—
Metabolic heat generation	$Q_{\text{met}}$ [W/m <sup>3</sup> ]	9265 <sup>#</sup>	3602 <sup>#</sup>	—
Porosity	$\phi$ [-]	—	20%	—
Diffusion coefficient in unbound interstitial fluid	$D_{n,f}$ [m <sup>2</sup> /s]	—	$9.57 \times 10^{-12}$	—
Regeneration coefficient	$B$ [-]	$9 \times 10^{-3}$	$9 \times 10^{-3}$	—

<sup>#</sup> Extracted from Infrared Imaging using Inverse Heat Transfer [Singh et al., 2020c] (33% larger perfusion rate than Lang et al., 1999).

### 2.2.3. Cell-necrosis induced interstitial-space enhancement: porosity computation

The interstitial space tends to increase with the cell-necrosis [Zhang et al., 2009] as;

$$\phi = \phi_o + (80\% - \phi_o)(1 - e^{-\Omega(x,y,z,t)}) \quad (16)$$

where,  $\phi_o$  is the initial volume fraction of the interstitial space before the heating. It is to note that as more and more tumour cells undergoes thermal cell-death ( $\Omega$ ), the tumour porosity tends to increase after

rupturing of cell membranes. It is assumed that tumour would approach a maximum of 80% enhancement in interstitial space. All thermophysical parameters are summarized in **Table-I**.

#### 2.2.4. Arrhenius kinetics of thermal cell-death: Arrhenius thermal damage computation

The classical Arrhenius kinetic rate equation used to capture the exponential intensification of thermal degradation of tumour tissue with the temperature time history can be written in differential form [Dombrovsky and Timchenko, 2015] as;

$$\frac{\partial \Omega(x, y, z, t)}{\partial t} = A_{bs}(1 - \Omega(x, y, z, t)) \exp\left(\frac{-E_{abs}}{R_u T(x, y, z, t)}\right) \quad \text{for } \Omega(0) = 0 \quad (17)$$

or it may be expressed in integral form [Singh et al., 2020] as;

$$\Omega(x, y, z, \tau) = \ln\left\{\frac{\zeta(0)}{\zeta(\tau)}\right\} = \int_0^\tau A_{bs} e^{-E_{abs}/R_u T(x, y, z, t)} dt \quad (18)$$

It was consistently reported by studies that the approximation of biological tissue coagulation by two parameters is a very rough estimation since the tissue not only consists of several proteins but also undergoes regeneration of healthy cells [Fasano et al., 2010; Dombrovsky et al., 2022]. To prevent any unrealistic protein denaturation, the thermal damage evaluated by traditional Arrhenius equation can be mathematically expressed as a piecewise function with a breakpoint or transitioning temperature occurring at 44°C.

$$\frac{\partial \Omega(x, y, z, t)}{\partial t} = \begin{cases} 0 & \text{for } T < 44^\circ\text{C} \\ A \exp\left(\frac{-E_a}{R_u T(x, y, z, t)}\right) & \text{for } T \geq 44^\circ\text{C} \end{cases} \quad (19)$$

This confirms that Arrhenius formulation may not accurately represent or over-predicts the thermal cell-death in initial stages of heating [Pearce et al., 2015; Singh et al., 2020]. The shortcomings of Arrhenius formulation in initial states of heating are corrected by Dombrovsky and Timchenko, 2015 by incorporating the concept of regeneration of tissues.

#### 2.2.5. Non-Arrhenius kinetics of thermal cell-death: Modified thermal damage computation

More recently, Dombrovsky and Timchenko, 2015 takes into account the regeneration of healthy tissues due to continuous supply of oxygen through arterial blood.

$$\frac{\partial \Omega(x, y, z, t)}{\partial t} = \underbrace{A(1 - \Omega(x, y, z, t)) \exp\left(\frac{-E_a}{R_u T(x, y, z, t)}\right)}_{\text{Arrhenius rate kinetics}} - \underbrace{B \omega_{c,0} \Omega(x, y, z, t)}_{\text{Regeneration term}} \quad (20)$$

where,  $\Omega$  is the degree of thermal destruction-burn injury,  $E_a$  is the activation energy,  $A$  is the frequency factor or pre-exponential factor. The kinetic rate coefficients can be referred from **Table-II**. The thermal damage parameter,  $\Omega = 1$  represents 63.21% of denaturation of proteins sufficient to initiate thermal coagulation and irreversible thermal cell-death.

### 2.2.6. Vascular-Stasis based blood perfusion computation

It is well known that during heating, the blood perfusion rate first increases at hyperthermic temperature due to vasodilation of vessels and then starts decreasing due to total collapse of vasculature following thermal damage. This phenomenon is known as “degree of stasis”. In this problem formulation, the blood perfusion of cancerous lesion is defined as a piecewise function of vascular stasis [He et al., 2004] as

$$\omega_{c,0}(t) = \begin{cases} \omega_{b,0}(1 + 30 \cdot \Theta); & \text{for } 0 < \Theta \leq 0.02 \\ \omega_{b,0}(1.86 - 13 \cdot \Theta); & \text{for } 0.02 < \Theta \leq 0.08 \\ \omega_{b,0}(0.884 - 0.79 \cdot \Theta); & \text{for } 0.08 < \Theta \leq 0.97 \\ \omega_{b,0}(3.87 - 3.87 \cdot \Theta); & \text{for } 0.97 < \Theta \leq 1.00 \\ 0; & \text{for } \Theta > 1.00 \end{cases} \quad (21)$$

This blood perfusion algorithm is illustrated pictorially in **fig. 4**. Here, the baseline value of blood perfusion,  $\omega_{b,0}$  (refer **Table-I**) is extracted from the thermal infrared imaging by adjusting the metabolic heat generation rates and blood perfusion values using inverse heat transfer analysis to match the thermal maps of infrared images [Singh et al., 2020c]. The degree of vascular stasis (collapse of vasculature) can be calculated as

$$\Theta(x, y, z, t) = 1 - \exp(-\xi(x, y, z, t)) \quad (22)$$

$$\xi(x, y, z, \tau) = \int_0^\tau A_{perf} \exp\left(\frac{-E_{a_{perf}}}{R_u T(x, y, z, t)}\right) dt \quad (23)$$

**Table-II:** Arrhenius coefficients considered in this study [Soni et al., 2015; Alzahrani and Abbas, 2019].

Parameters	Symbol [Units]	Vascular Stasis	Thermal damage
Frequency factor	$A$ [ $s^{-1}$ ]	$1.98 \times 10^{106} \ddagger$	$3.1 \times 10^{98} \ddagger$
Activation Energy	$E_a$ [ $Jmol^{-1}$ ]	$6.67 \times 10^5 \ddagger$	$6.28 \times 10^5 \ddagger$

$\ddagger$ bulk tissue skin:  $A_{bs}$  and  $E_{abs}$

$\ddagger$ biological tissue with capillaries:  $A_{perf}$  and  $E_{a_{perf}}$

Remark 1: It is to note that the Arrhenius coefficients employed to evaluate blood perfusion changes are unrelated to the ones used for thermal cell-death.

### 2.3. Boundary conditions

- (i) During actual experiment, the mouse was kept on thermal pad to maintain and mimic the constant body temperature of human body. Therefore, the bottom surface of mouse in touch with pad is imposed with Dirichlet boundary condition,  $T_{\text{pad}} = 37^{\circ}\text{C}$ .
- (ii) The Neumann boundary conditions are considered at malignant – healthy tissue interface. The heat flux coming from the malignant tissue is completely received by the healthy tissue region. The continuity of heat fluxes is imposed at tumour-healthy region interface i.e.  $k \cdot \nabla(T)_{\text{tumour tissue}} = k \cdot \nabla(T)_{\text{healthy tissue}}$ .
- (iii) Lumped heat transfer coefficient ( $\bar{h}_{\text{lumped}} = 5.13 \text{ W/m}^2\text{K}$ ) is extracted from infrared imaging using inverse heat transfer. Tumour geometry is assumed as near spherical and mouse body as cylindrical. Convective heat transfer coefficient from Newton's law of cooling as well as radiation heat transfer coefficients from Stefan-Boltzmann's law are employed to match the temperatures of thermal infrared imaging to compute blood perfusion and nominal metabolic heat generation rate [Singh et al., 2020c]. Complete implementation is covered in forthcoming work under review [Singh et al., 2022].
- (iv) A no-flux boundary condition at the tumor boundary is prescribed for concentration equation, considering that nanoparticles are unlikely to migrate to the tumor surface during the time duration of the heating.

#### 2.4. Numerical procedure

A four-way coupled heat transfer problem was solved using a numerical computational platform, COMSOL Mutiphysics software v. 5.2 (COMSOL Inc., AB, Stockholm, Sweden). It is worth to note that the thermophysical parameters such as density, thermal conductivity, specific heat capacity blood perfusion, are considered as isotropic. The computational domains such as PC3 tumour and mouse body has been discretized well into heterogeneous tetrahedral elements using customized inbuilt mesh generator features of COMSOL that provides user-defined meshing size options based on the maximum element growth rate, curvature factor, minimum element size, maximum element size, and resolution of narrow region. The mesh convergence analysis or Grid Independency test has been very precisely conducted to determine the optimal number of meshing elements and its sensitivity for reducing the computational cost of simulation experiments and to ensure that the simulation results are independent of number of meshing elements. The mesh is optimized until the variation in results is less than 0.1%. The pre-specified relative tolerance of 0.01 for the biological heat transfer has been set to sixth-order 0.000001 for achieving a numerical convergence. The tetrahedral elements are used to discretize the physical domain and the quadratic lagrangian elements are used to discretize the solution space. The Newton-Raphson algorithm has been used with MUMPS iterative solver. The numerical computations have been performed on a T7500 Dell Precision machine with Processor: Intel® Xeon® CPU E5507 @2.27GHz, 2.26GHz (2 processors) with 35 GB Installed RAM on a 64-

bit operating system, x64-based processor. It took an average of 92 hours to compute the solution of the biophysics problem solved via five-segregated steps taken by solver.

### 3. Results

A four-way coupled simulation framework has been extensively studied for heterogeneous distribution of magnetic nanoparticles [LeBrun et al., 2016b; Singh et al., 2020; Singh et al., 2021] by inclusion of vascular-stasis governed blood perfusion changes [Schutt and Hammerich, 2008; Prakash and Diederich, 2012; Soni et al., 2015] with regeneration of healthy cells [Dombrovsky and Timchenko, 2015; Dombrovsky, 2019; Dombrovsky, 2022] during heating. The temperature computed from Pennes bioheat equation is employed to predict heat-induced thermal cell-injury using Arrhenius equation. The computed thermal damage is then used to update the porosity. The interstitial space enhancements with thermal damage is used to evaluate the diffusion coefficient. The diffusion coefficient and interstitial volume fraction are present in concentration equation, hence, thermal damage induced changes will affect the concentration distribution of nanoparticles. The external heat generation source term is concentration dependent and is updated at each time step in concentration equation. Here, the perfusion is expressed as a function of microvascular stasis which is linked to temperature time history.

To monitor the response of nanoparticle assisted thermal therapy, temperature probes are placed at minimal temperature location between the interface of tumour and healthy tissue and maximum temperature location at highly concentrated nanoparticle regions. The probe locations can be retrieved from the meshing coordinates by applying Euclidean distance approach. These locations are dynamically monitored during heating using thermal probes to ensure sufficient damage front have been developed as per the proposed heating protocols reported in literature [LeBrun et al., 2016b; Singh et al., 2020; Dombrovsky and Timchenko, 2015]. For the present case scenario, the volume temperature minimum location ( $T_{min}=48.463^{\circ}\text{C}$ ;  $x=0.0030102$  m,  $y=0.0036869$  m,  $z=1.8488 \times 10^{-4}$  m) lies at the tumour region embedded within the healthy mouse domain. The volume temperature maximum location ( $T_{max}=83.123^{\circ}\text{C}$ ;  $x=5.5852 \times 10^{-4}$  m,  $y=0.0038334$  m,  $z=0.0087127$  m) lies at highly concentrated nanoparticle regions mostly towards the surface. At the interface region of PC3 tumour and healthy tissue, burns of moderate intensity are expected due to dominance of heat conduction phenomenon. All accumulated heat radially traverse in all directions. However, major heat dissipation is towards the contact surface.

It is to note that during the initial stages of heating, the spread of heat generation dominate the thermal gradients in the near vicinity of nanoparticles. Heat generation from these zones varies as a function of distance and mathematically expressed at a rate proportional to  $r^3$ , where  $r$  being the distance from heating zone. Conversely, it can be stated as the rate at which heat is transferred across the tumour-healthy tissue extremities depends on tumour surface area (i.e. rate is proportional to  $r^2$ ) [Xu et al., 2009].

Due to this radial spreading of heat from magnetic nanoparticles in the presence of alternating magnetic field, the heating of healthy tissue fringes around the tumour seems to be a slow process at the minimum temperature location as evident from **figs. 2** and **3**. This region always take longer time to achieve a minimal therapeutic index.

The focus is on minimum temperature location because (i) firstly, this location particularly acts as a heat sink and takes longer time to achieve a minimal therapeutic damage index. Cold-spots usually occurs at these zones. Furthermore, these lowest temperature zones (minimally ablated regions) may cause recurrence of cancerous cells i.e. tumours have the potential to appear back at this heating site if remain untreated, (ii) secondly, the heat loss is maximum at this region due to the prevalence of compensatory thermoregulation mechanisms of healthy tissues, (iii) thirdly, evident rise in blood perfusion levels before the functional blood supplying vessels gets collapsed. This aspect is also taken care in present study by modelling perfusion as a function of vascular stasis. Blood perfusion term contributes for convective heat transfer between the biological tissue and blood, (iv) lastly, the regeneration of healthy cells counters heat coming from tumour. However, it is always the point of concern i.e. How enough is too enough? or how minimum is too minimum?

**Fig. 2** illustrates spatio-temporal variation of four notable therapeutic parameters namely temperature, thermal damage, vascular stasis and blood perfusion after one-hour of exposure at minimal temperature location. These parameters are shown in **fig. 3** at end treatment point for center-slice of tumour and healthy tissue at interface. It can be inferred from **fig. 4** that the maximum peak of perfusion is achieved at threshold temperature of 43.5°C. Perfusion collapse at this treatment location takes place at 1750 sec. The volumetric temperature maximum of  $T_{max} = 83.13^{\circ}\text{C}$ , temperature minimum of  $T_{min} = 48.46^{\circ}\text{C}$ , and temperature average of  $T_{avg} = 67.23^{\circ}\text{C}$  is achieved after one hour of heating. On evaluation of “Source maps” (before heating) with “Destination maps” (after heating) suggests five-fold increase in diffusion coefficient from nominal value of  $9.57 \times 10^{-12} \text{ m}^2/\text{s}$  to  $4.87 \times 10^{-11} \text{ m}^2/\text{s}$ . Here, migration distance,  $L$  relates to diffusion coefficient,  $D_n$  and time,  $t$  as  $L = \sqrt{D_n t}$ . Hence, damage causes the thermal enhancements in tumour porosity to proportionally enhance the diffusion thus, causing migration of nanoparticles. It is noticeable from **fig. 5** that there is 39.62% increase in redistribution volumes of nanoparticles. The scientific reasoning for such enhancement in interstitial space is attributed to the fact that dead cells release intracellular solution after the rupturing of cell membrane to create migration path for particles to diffuse more freely.

Here, the nanoparticle distribution volume is defined in the entire tumour as a region containing a nanoparticle concentration  $\geq 10\%$  of the maximal nanoparticle concentration [**Singh et al., 2021b**]. The volumetric concentration maximum of  $2311.11 \text{ mol}/\text{m}^3$  is used as a criterion to compute the nanoparticle distribution volumes for different concentration ranges of 10-21%, 21-34%, 34-45%, 45-100%.

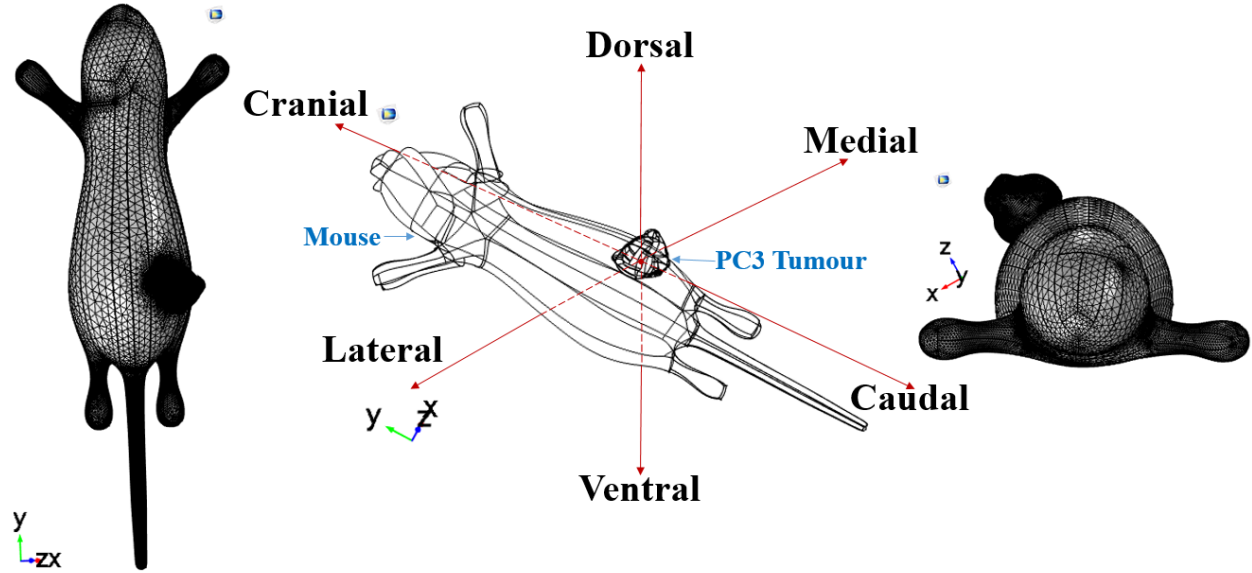


Fig. 1. Geometrical description and wireframe model of biological tissue domains. Irregular PC3 tumour is attached to the same flank position to mimic the experiments.

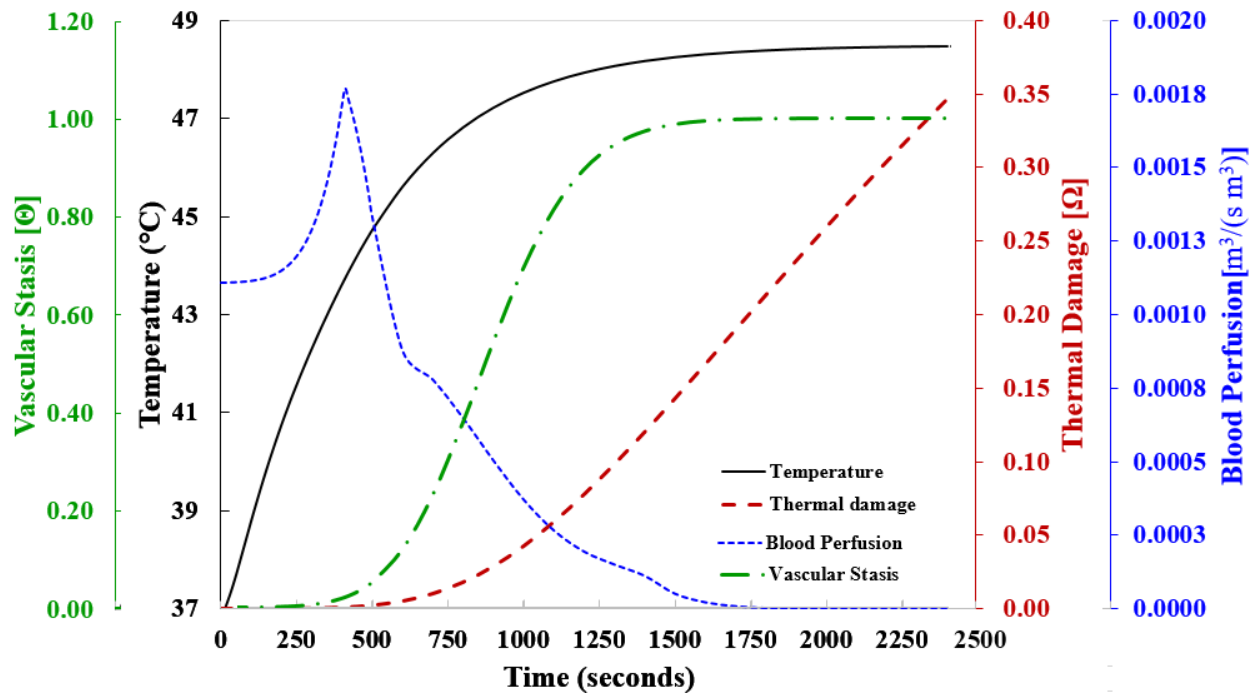
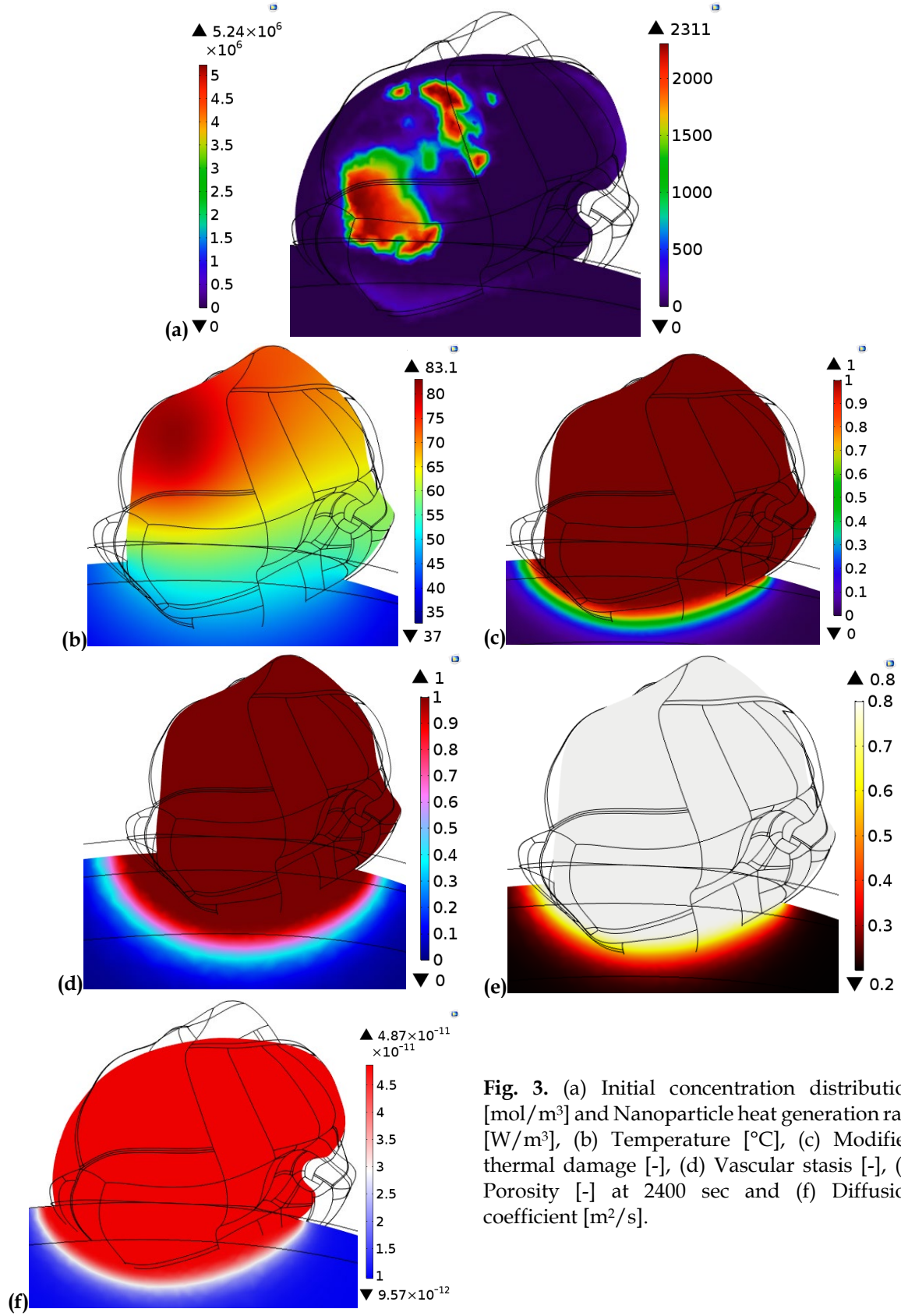


Fig. 2. Illustration of propagation of modified thermal damage front with regeneration of healthy cells, Vascular-Stasis governed perfusion, Vascular Stasis and Temperature with time at the minimal temperature probe (sensor) position. It is evident that the thermal damage restrict within bounds of  $\Omega \leq 1$ . The inclusion of regeneration term suppress the thermal damage to propagate within the healthy tissue fringes surrounding tumour. Vascular stasis (collapse of vasculature) is developed late at the interface of tumour and healthy tissue follows the perfusion algorithm reported in literature. The complete vascular stasis ( $\Theta=1$ ) is achieved at almost 1250 sec. Complete vascular shut- down is achieved at almost 1750 sec after exposure of magnetic nanoparticles to alternating magnetic fields. Perfusion shows an initial increase and slowly decreasing with the damage. This is a highly coupled system taking into account dependence of parameters on each other.





**Fig. 3.** (a) Initial concentration distribution [mol/m<sup>3</sup>] and Nanoparticle heat generation rate [W/m<sup>3</sup>], (b) Temperature [°C], (c) Modified thermal damage [-], (d) Vascular stasis [-], (e) Porosity [-] at 2400 sec and (f) Diffusion coefficient [m<sup>2</sup>/s].

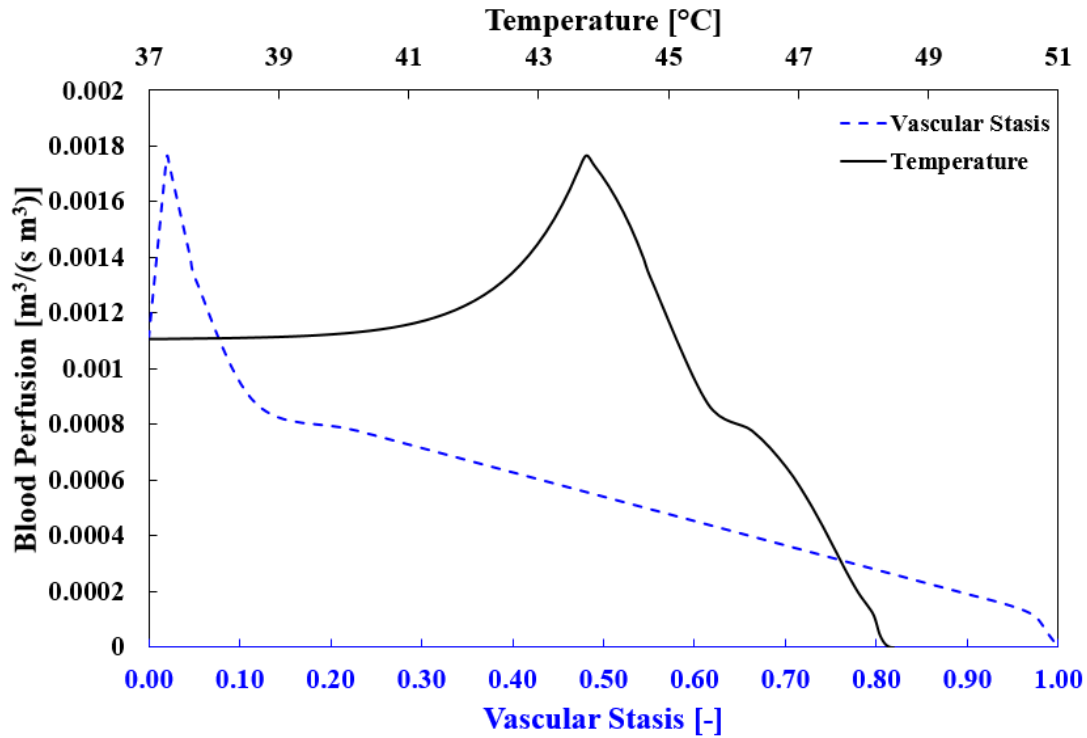


Fig. 4. Illustration of functional dependence of blood perfusion on vascular stasis and temperature at minimal temperature location at interface.

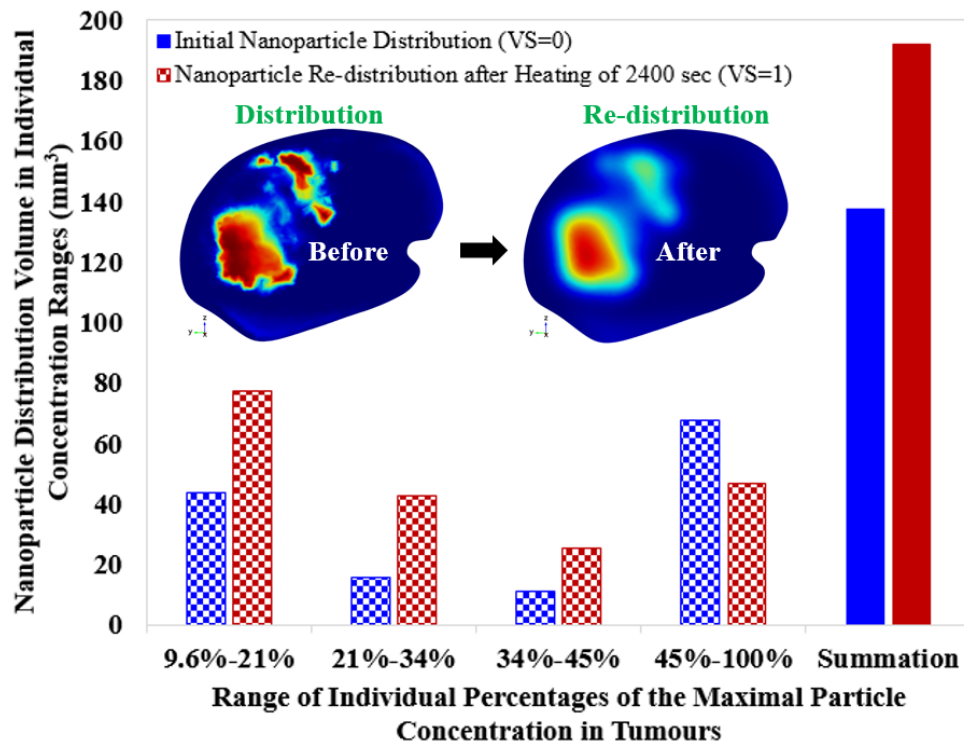
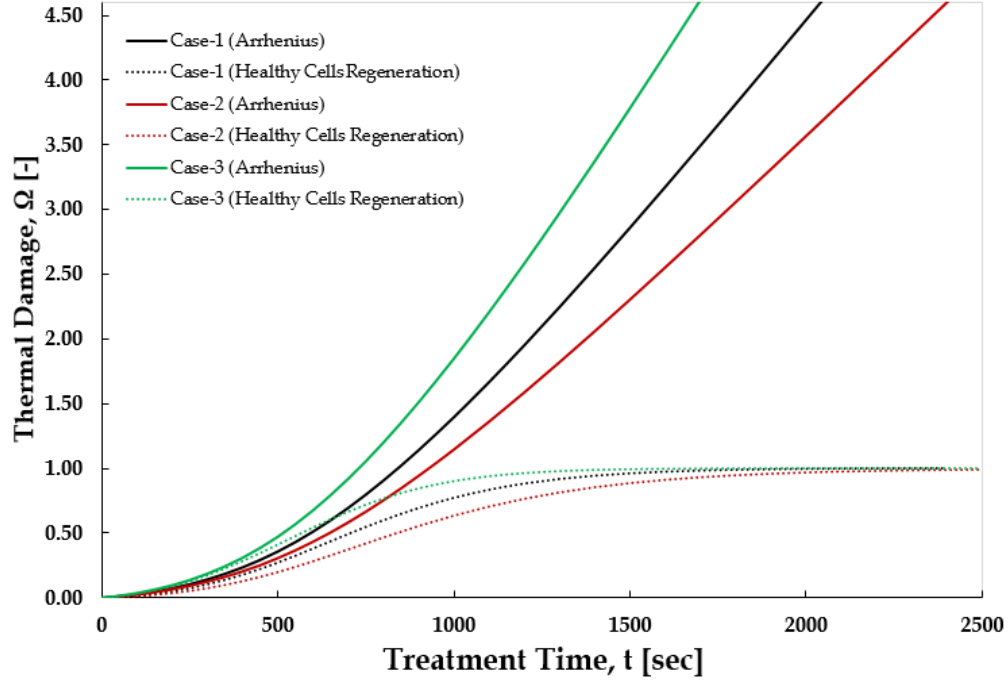
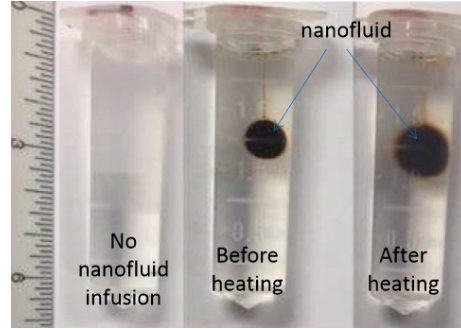


Fig. 5. Nanoparticle distribution comparison before and after heating. For a 5.8% injection of magnetic nanoparticles, the maximum concentration from microCT extracted region is found to be 2311.11 mol/m<sup>3</sup>. There is 39.62% rise in nanoparticle distribution volumes. Magnetic nanoparticles migrates from the region of higher concentration to the region of lower concentration. Here, VS implies Vascular Stasis.

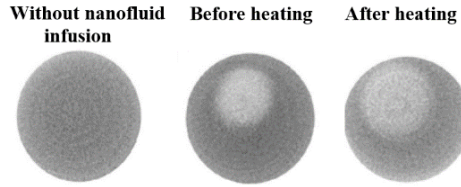


**Fig. 6.** Comparative analysis of Healthy Cells Regeneration model with Arrhenius model. Three set of Arrhenius kinetic coefficients are additionally plotted for Arrhenius and non-Arrhenius kinetics of thermal cell-death. Case 1:  $E_a = 2.38 \times 10^5$  [J/mol] (for  $T \leq 54^\circ\text{C}$ ) and  $1.24 \times 10^5$  [J/mol] (for  $T > 54^\circ\text{C}$ ),  $A = 1.8 \times 10^{36}$  [1/s]; (for  $T \leq 54^\circ\text{C}$ ) and  $7.0 \times 10^{17}$  [1/s] (for  $T > 54^\circ\text{C}$ ); Case 2:  $E_a = 2.318 \times 10^5$  [J/mol],  $A = 1.19 \times 10^{35}$  [1/s]; Case 3:  $E_a = 2.222 \times 10^5$  [J/mol],  $A = 6.75 \times 10^{33}$  [1/s]. Arrhenius model over-predicts thermal cell-death while regeneration model suppress thermal damage. However, both models relates to temperature–time history. Thermal damage profiles for both models are in congruence with the results of **Liu and Chen, 2021**.

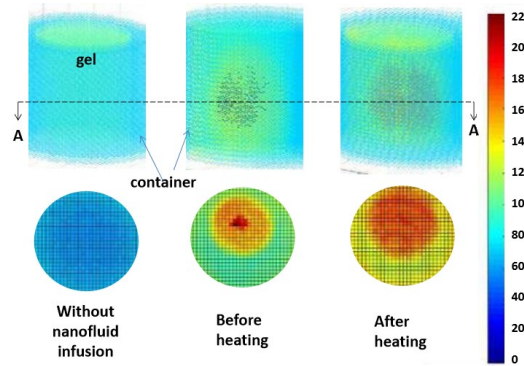
In this work, Arrhenius and Non-Arrhenius kinetic models of thermal cell-death are compare and contrast. After implementation of these thermal cell-death models, we found that the thermal damage estimated by the modified Dombrovsky model in the tumour is lower than that estimated by first order Arrhenius formulation which is in agreement with the findings reported by **Liu and Chen, 2021**. Following the contours of **fig. 2**, it would certainly be true to remark that the regeneration mechanism triggers an immune response of biological tissue towards continued heating. It shows a very close agreement with the seminal work of **Dombrovsky and Timchenko, 2015; Dombrovsky, 2019; Dombrovsky, 2022** on regeneration. Furthermore, three set of Arrhenius kinetic coefficients are additionally plotted in **fig. 6**. We conclude that the inclusion of regeneration term with microvascular perfusion seems to suppress, prevent and restrict the thermal damage to propagate within the healthy tissue fringes surrounding tumour. Therefore, any further accumulation of thermal damage would remain within bounds of  $\Omega \leq 1$ . The physical interpretation of this suppression is that it tends to save the intact tissue layers by supplying more oxygen and blood perfusion to the injury site thereby saving critical adjoining tissues.



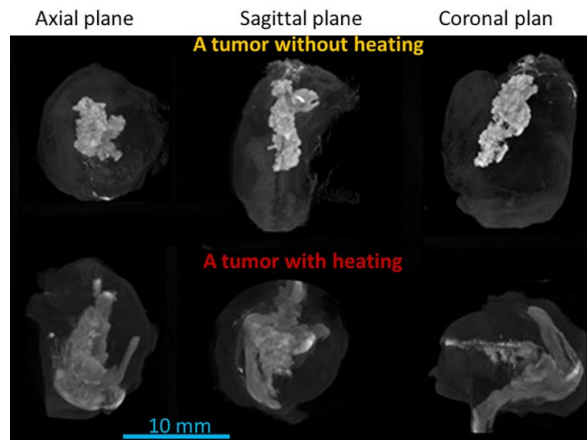
(a) Agarose gel with or without nanofluid injection



(b) MicroCT slices of agarose gel specimens



(c) 3D color contours of nanoparticle distribution in gels before and after heating



(d) PC3 tumours with and without heating demonstrating re-distribution of magnetic nanoparticles

Fig. 7. (a) *In-vitro* experimental work on tissue equivalent agarose gels, (b) microCT slices, (c) thermal simulations on agarose gels and (d) *In-vivo* Maximum Intensity Projection (MIP) images of two tumors in the axial (left), sagittal (middle), and coronal (right) planes. The tumors were injected with 0.1 cc ferrofluid at an infusion rate of 3  $\mu\text{L}/\text{min}$ , top depicts a tumor in the control group without heating; and bottom depicts a tumor in the heating group with 25 min of heating [adapted from the work of Gu et al., 2017; Gu et al., 2019].

### 3.1. Validation of the coupled modeling approach

Experimental validation for the performed simulations have been verified through *in-vitro* tissue-equivalent agarose gel phantom studies (refer **fig. 7(a-c)**) [Gu et al., 2017], or *in-vivo* animal studies [Gu et al., 2019] (refer **fig. 7(d)**). One study have suggested that nanoparticle migrates from higher concentration regions to lower concentration regions due to thermal diffusion resulting in possible re-distribution known as “thermal by-stander effect” [Jordan et al., 1997]. Blood perfusion variation with time as shown in **fig. 2** mimics the results of Soni et al., 2015. Our findings of healthy cells regeneration are in agreement with the results of founding authors Dombrovsky and Timchenko, 2015; Dombrovsky, 2019; Dombrovsky, 2022 and implemented works of Liu and Chen, 2021.

## 4. Discussion

The modification to the first order Arrhenius kinetic rate equation was first proposed by Dombrovsky and Timchenko, 2015; and later revisited by Kumar and Rai, 2016. It was recently implemented by Liu and Chen, 2021 which accounts for regeneration of the healthy cells through an additional regeneration term to the RHS of the traditional Arrhenius equation. The more explanation to the regeneration capabilities of living biological tissues during hyperthermia treatment were further elaborated and discussed in the works of Dombrovsky, 2022; Dombrovsky, 2019. It should be noted that the induced thermal damage is zero before the onset of nanoparticle assisted heating. According to the hypothesis of Dombrovsky and Timchenko, 2015; continuous regeneration of living human tissues is attributed to the continuous supply of oxygen through arterial blood must be taken into account to counter balance the thermal degradation at quasi-static thermal conditions. The same concept can be equally postulated for tumour tissue. Hence, according to their hypothesis, the traditional Arrhenius equation based thermal damage estimations over-predicts the thermal signatures of cell-death to surrounding host tissue within several-tens of minutes of thermal treatment. This conjecture was supported by Liu and Chen, 2021 who explicitly states that the regeneration term tends to suppress the thermal cell-death at the interface of tumour and healthy biological tissue. Furthermore, the Dombrovsky, 2022 affirms that while modelling the kinetics of thermal damage of tumour, one must include and should not ignore the partial self-regeneration of connecting normal human tissues at the tumour periphery due to continuous matching of oxygen demands in the healthy tissue through arterial blood [Collins et al., 2015]. Whole body heat transfer models confirms the validity of the imposed modification of Arrhenius equation. Hence, thermo-regulation governed phenomenon occurring during hyperthermia heating as highlighted by Dombrovsky and Timchenko 2015; Dombrovsky, 2019; Dombrovsky, 2022 seems to be intuitively correct and physically reasonable. However, this interesting issue which was never accounted for in thermal simulations by researchers must be included in *priori* simulation treatment planning. Thus, we can suspect qualitatively

correct results, since oxygen-rich arterial blood will only be supplied to the healthy tissue fringes surrounding the tumour tissue since the potential blood supply to tumour seemingly missing due to parallel initiation of vascular-stasis (collapse of vasculature), mathematically expressed as “*degree of stasis*”,  $\Theta$ . Thus, it may be inferred that implementation of regeneration of healthy tissues will prevent damage to penetrate deeper inside the connective tissue layers as over-predicted by Arrhenius equation and hence, improvised estimates can be expected from non-Arrhenius kinetics. One-stage Arrhenius thermal damage model typically exhibits an error margin of 15-20% in comparison to two-state model which exhibits 3-5% error margin. Pearce thermal damage model improves shortcomings of Arrhenius model by addressing slowly developing shoulder region and heating treatment time reductions by 24% [Singh et al., 2020].

Controlled spatial distribution of magnetic nanoparticles is an outcome of controlled infusion strategies [LeBrun et al., 2016a]. We conform our analysis for a controlled infusion rate of 3  $\mu\text{L}/\text{min}$  based on 5.8% nanoparticle dose loadings consistent to the previous experimental works [LeBrun et al., 2016b]. We need to emphasize here that the aim of thermal ablation is to fully encompass the cancerous lesion with minimum collateral damage of healthy tissues [Singh et al., 2021a]. Most of the researchers confine their discussions to optimize the heating treatment time that depends on infusion rate and distribution of nanoparticles [Singh et al., 2020]. In addition to this, we have introduced here three modelling advancements namely heating induced redistribution, healthy cells regeneration, and cell-necrosis induced enhancement in tumour porosity (CNIPE) and diffusion diffusivity (CNIDC), choice of mathematical model employed to capture vascular-stasis induced perfusion changes. It is certainly true to remark that increasing the infusion rate leads to an increase in nanoparticle penetration depths in cancerous lesion [Darvishi et al., 2021]. They reported that by increasing the infusion rate 10 times from 4  $\mu\text{L}/\text{min}$  to 40  $\mu\text{L}/\text{min}$  results in 17% increase in penetration depth. Another experimental work reports 50% increase in penetration depths by increasing the infusion rate to double from 5  $\mu\text{L}/\text{min}$  to 10  $\mu\text{L}/\text{min}$  [Attaluri et al., 2011]. However, the outcome of increased infusion rates reveals counterintuitive findings, necrosis will primarily occur in healthy tissue rather than cancerous tissue. The location of necrosis recedes from the tumour center and approaches the boundaries of tumour (crack formation) and healthy tissue interface [Singh et al., 2021d]. Our claims of choosing lower infusion rate of 3  $\mu\text{L}/\text{min}$  is in congruence with Darvishi et al., 2021 who conclude 1.25  $\mu\text{L}/\text{min}$  as an infusion strategy.

The blood perfusion rate of tumour is found to be smaller than healthy tissue. It is because the vascular system of tumour remains undeveloped and inefficient due to its typical chaotic structure. However, we have assumed that blood supplying capillaries are present all over the tumour tissue. Therefore, it seems reasonable to capture the variation of perfusion as a function of vascular stasis. The baseline blood perfusion rate used in this work is extracted from infrared imaging using inverse heat transfer analysis. The extracted blood perfusion for the tumour and mouse are adjusted until there is a close fit to the average tumour tissue temperature and the selected mouse region is achieved. The extracted blood

perfusion value of 0.0011079 [1/s] seems to be 33% larger than the mostly accepted value of the work of **Lang et al., 1999**; however, the order of magnitude is found to be same. For such infrared imaging assisted perfusion mapping, coupling of metabolic heat generation term and perfusion term is assumed for such formulation.

One should note that the vascular stasis influenced blood perfusion appears in the regeneration term on the RHS of **equation 20**. Therefore, the inclusion of stasis based blood perfusion also tends to suppress the thermal damage and acts as a sink. The vascular collapse starts at the highly concentrated regions of magnetic nanoparticles and slowly progressing towards the interface of tumour and healthy tissue.

Thermal diffusion of heat by nanoparticles helps to develop an envelope of ablation around cancerous lesion. The healthy tissue fringes (5–10 mm) adjacent to the tumour must be heated within the temperature range of 50–55°C in order to achieve 63.2% transformation or denaturation of proteins - an indicator of thermal damage index of 1. It is substantial to sacrifice those healthy tissue layers in order to avoid recurrence of cancerous cells [**Singh et al., 2021a**]. Although it is very difficult to maintain such thermal distribution due to prevailing perfusion conditions. Blood perfusion in these adjacent fringes is slightly higher in comparison to normal tissue lying remote from the tumours. This notion is supported by the experimental findings for Walker 256 carcinoma in male Sprague-Dawley rats for which the blood flow in the skin and muscle tissue adjacent to tumour was approximately two times larger than skin and muscle tissue of normal leg [**Song et al., 1980**]. While for Fischer rats, it shows a 7.5 fold and 3.5 fold increase adjacent to mammary adenocarcinoma 13762A [**Rappaport and Song, 1983**]. This is the reason, why the intact layers of tumour tissue takes much longer time to achieve uniform thermal damage.

This model conforms to the assumption that tumours located near the superficial skin tissue layers have relatively thin blood supplying vasculature and capillaries. Contrary to this, at deeper tissue regions, larger blood supplying arteries might be present due to which thermal degradation of erythrocytes supplied by arterial blood is very difficult to achieve. One has to note that, our microCT imaging extracted PC3 tumour is attached to the same flank position in superficial tissue layers mimicking experimental mice [**Singh et al., 2020**]. We envisage that magnetic nanoparticles undergoes redistribution during heating may increase the interstitial space of tumour, thus, allowing the nanoparticles to diffuse and traverse to larger trajectory paths. For such redistribution phenomenon, the heating time is sufficient to reduce the oxygen in erythrocytes (red blood cells) and maximize the thermal damage.

The treatment efficacy of magnetic nanoparticles induced heating depends on the time required by whole tumour to achieve thermal alterations that are sufficient to induce thermal-cell injury. In future, Arrhenius equation can further be modified by adding kinetic rate coefficients before the exponent (Activation energy and pre-exponential factor) to accommodate the loss of oxygen by erythrocytes during arterial blood heating. However, further experimental work is needed in this direction.



It is to note that oxygen regeneration capabilities of tumour tissue unlike healthy tissue may result in asphyxiation of the tumour (depriving of oxygen) following vascular disruption of capillaries during heating. Due to this asphyxiation process, oxidative stress triggered mechanisms of hemolysis (rupturing of red blood cells) may occur spontaneously during Neél relaxation heating of nanoparticles. According to **Gershfeld and Murayama, 1988**, unilamellar state of cell membrane is stable at 37°C but for erythrocytes, unilamellar-multibilayer transformation which is a manifestation of hemolysis occurs at relatively mild temperatures i.e. between 38 and 45°C [**Singh et al., 2021c**]. Hence, thermally induced hemolysis with temperatures exceeding >45°C may invoke processes: (a) Vital enzymes inactivation with denaturation or deterioration of structural proteins, (b) formation of lytic agents in plasma leading towards membrane disorganization with the release of cellular macromolecules (melting of membrane lipids and becomes leaky). The activation energy of 80 kcal/mole for temperatures >45°C is 2.76 fold higher than the energy of activation at mild temperatures. Future work will extend this spectrum of work towards patient-specific anatomies [**Singh, 2016**].

The thermal damage accrued in Arrhenius damage model is incapable of modelling damage production rates of exactly zero order magnitude thereby suggesting that damage integral might have already grown by almost 80% in accordance to Arrhenius equation. This statement is in concordance with the claims of **Van de Sompel, 2009** suggesting that for temperatures below 45°C, the damage production rates become physiologically insignificant. For such claims of temperatures < 45°C, we envisage that the regeneration of biological tissues presents physiologically relevant reductions in accrued damage injury. Hypothetically, the benefits of regeneration is to suppress thermal damage accumulation over time thereby reducing the penetration depth of the burn. At interface region, burns of moderate intensity are expected due to dominance of heat conduction phenomenon. The true damage accrued in such regions is appreciably smaller of the order of  $10^{-7}$  in comparison to first degree burn threshold value of  $\Omega = 0.53$  and much smaller in comparison to second degree threshold injury of  $\Omega = 1$ .

We plan to test this hypothesis in future computational experiments for range of Arrhenius coefficients (pre-exponential factor -  $A$ , and apparent activation energy -  $E_a$ ). It is of great interest to study the extent of incurred injury for a given burn injury protocol with the experimental data considering specific burn times, burn criteria, temperatures and adopted models of cell-death with monotonic non-linear functions and proposed extrapolations. For skin tissue alone, several injury coefficients have been proposed and tested in literature namely **Henriques, 1947**:  $E_a = 6.27 \times 10^5$  [J/mol],  $A = 3.1 \times 10^{98}$  [1/s]; **Fugitt, 1955**:  $E_a = 6.27 \times 10^5$  [J/mol] (for  $T \leq 55^\circ\text{C}$ ) and  $2.96 \times 10^5$  [J/mol] (for  $T > 55^\circ\text{C}$ ),  $A = 3.1 \times 10^{98}$  [1/s] (for  $T \leq 55^\circ\text{C}$ ) and  $5.0 \times 10^{45}$  [1/s] (for  $T > 55^\circ\text{C}$ ); **Stoll and Greene, 1959**:  $E_a = 7.82 \times 10^5$  [J/mol] (for  $T \leq 50^\circ\text{C}$ ) and  $3.27 \times 10^5$  [J/mol] (for  $T > 50^\circ\text{C}$ ),  $A = 2.185 \times 10^{124}$  [1/s] (for  $T \leq 50^\circ\text{C}$ ) and  $1.823 \times 10^{51}$  [1/s] (for  $T > 50^\circ\text{C}$ ); **Takata, 1974**:  $E_a = 4.18 \times 10^5$  [J/mol] (for  $T \leq 50^\circ\text{C}$ ) and  $6.69 \times 10^5$  [J/mol] (for  $T > 50^\circ\text{C}$ ),  $A = 4.322 \times 10^{64}$  [1/s] (for  $T \leq 50^\circ\text{C}$ ) and  $9.389 \times 10^{104}$  [1/s] (for  $T > 50^\circ\text{C}$ ); **Wu, 1982**:  $E_a = 6.27 \times 10^5$  [J/mol]



(for  $T \leq 50^\circ\text{C}$ ) and  $6.27 \times 10^5 - 5.10 \times 10^5 (T - 53)$  [J/mol] (for  $T > 50^\circ\text{C}$ ),  $A = 3.1 \times 10^{98}$  [1/s] (for  $T \leq 50^\circ\text{C}$ ) and  $3.1 \times 10^{98}$  [1/s] (for  $T > 50^\circ\text{C}$ ). For PC3 cell type, **Rylander et al., 2010**:  $E_a = 2.38 \times 10^5$  [J/mol] (for  $T \leq 54^\circ\text{C}$ ) and  $1.24 \times 10^5$  [J/mol] (for  $T > 54^\circ\text{C}$ ),  $A = 1.8 \times 10^{36}$  [1/s] (for  $T \leq 54^\circ\text{C}$ ) and  $7.0 \times 10^{17}$  [1/s] (for  $T > 54^\circ\text{C}$ ); **Feng et al., 2008**:  $E_a = 2.318 \times 10^5$  [J/mol],  $A = 1.19 \times 10^{35}$  [1/s]; **Pearce, 2015**:  $E_a = 2.222 \times 10^5$  [J/mol],  $A = 6.75 \times 10^{33}$  [1/s], **Talaee and Kabiri, 2019**:  $E_a = 1.67 \times 10^5$  [J/mol],  $A = 3.55 \times 10^{24}$  [1/s].

In future we plan to incorporate a relevance function -  $\Xi$  through normalized logarithmic transformed damage field,  $\log(\Omega_b)$  which can be expressed as,  $\Xi = \frac{\Omega_{final} - \Omega_b}{\Omega_b} \cdot \frac{[\log_{10}(\Omega_b) - \min(\log_{10}(\Omega_b))]}{[\max(\log_{10}(\Omega_b)) - \min(\log_{10}(\Omega_b))]}$ . It is a heuristic estimate that describes the relationship between exponential increase in  $\Omega_b$  and steady increase in true injury levels or physiological burn severity. Here,  $\Omega_b$  is the accrued damage at the point of switching off the alternating magnetic field,  $\Omega_{final}$  is the total accrued damage. This relevance function may also cause significant reductions in damage.

## 4. Conclusions

The inclusion of regeneration of living tissues to compute the thermal signatures of cell-death suggests that the modified Arrhenius equation seems to restrict within the damage limits of  $\Omega = 1$  (63.21% denaturation of protein). The physical interpretation of this regeneration term implies that thermal damage would not propagate deep inside the healthy tissue fringes. Thus, it can be inferred that regeneration phenomenon prevents and suppresses the collateral thermal damage spread at the interface which is in congruence with previous published works. We speculate that for a tumour needs to be treated within the hyperthermic temperature range, it will not only predict accurate ablation volumes but also restricts the damage propagation front to cross the fringe layers at the interface of tumour and healthy tissue. Such a model based on vascular shunt-off is a real assessment of the thermal damage spread within bounds of  $\Omega \leq 1$ . For the deadliest cancers like Glioblastomas, or chest wall recurrence (CWR) where the clinical margins are not enough to be sacrificed, these estimates will aid in better treatment planning. By adopting the proposed approach, damage can be maximized in the necrosis zones of tumour and minimized in the adjoining healthy tissues.

Incorporating the regeneration effect to estimate the thermal cell-death is a very novel implementation but it is still an undeveloped area that warrants further experimental investigation. Extended clinical studies will be needed to reach a firm conclusion and to elucidate any additional confounding factors such as influence of Heat Shock Proteins (HSPs). In nutshell, the biological signatures of thermal damage injury reach may seem to be intuitively correct but we still consider this as a subjective definition and the issue needs further attention to design more objective and reproducible methods to quantify regeneration phenomenon.

## Funding

This research did not receive any specific grant from any funding agencies in the public, commercial, or not-for-profit sectors.

## Acknowledgements

M.S. wish to acknowledge the support of Dr. Liang Zhu, Department of Mechanical Engineering, College of Engineering and Information Technology, University of Maryland Baltimore County, Baltimore, Maryland, USA for providing computational facilities and infrastructure support. Manpreet Singh is also thankful to the Graduate School, University of Maryland, Baltimore County for conferring the award of Dissertation Fellowship towards the progress of Doctorate degree.

## Declaration of Competing Interest

The author declare that there is no known competing financial interests or personal relationships that could have appeared to influence the work reported in this paper.

## ORCID

Manpreet Singh <https://orcid.org/0000-0003-2134-9271>

## References

- 1 L.A. Dombrovsky, Laser-induced thermal treatment of superficial human tumors: An advanced heating strategy and non-Arrhenius law for living tissues, *Frontiers: Frontiers in Thermal Engineering*, 1 (2022), pp. 807083.
- 2 L.A. Dombrovsky, V.M. Timchenko, Laser induced hyperthermia of superficial tumors: Computational models for radiative transfer, combined heat transfer, and degradation of biological tissues, *Thermal Process Engineering* 7 (1) (2015), pp. 24–36 (in Russian).
- 3 L.A. Dombrovsky, Scattering of radiation and simple approaches to radiative transfer in thermal engineering and biomedical applications, in *Springer Series in Light Scattering*, Editor A. Kokhanovsky (Cham (Switzerland): Springer Nature), 4 (2019), pp. 71-127.
- 4 D. Kumar, K.N. Rai, A study on thermal damage during hyperthermia treatment based on DPL model for multilayer tissues using finite element Legendre wavelet Galerkin approach, *Journal of Thermal Biology* 62 (2016), pp. 170-180.
- 5 K.-C. Liu, T.-M. Chen, Comparative study of heat transfer and thermal damage assessment models for hyperthermia treatment, *Journal of Thermal Biology* 98 (2021), pp. 102907.
- 6 P. Prakash, C.J. Diederich, Considerations for theoretical modelling of thermal ablation with catheter-based ultrasonic sources: Implications for treatment planning, monitoring and control, *International Journal of Hyperthermia* 28 (1) (2012), pp. 69-86.

- 7 D.J. Schutt, D. Haemmerich, Effects of variation in perfusion rates and of perfusion models in computational models of radio frequency tumor ablation, *Medical Physics* 35 (8) (2008), pp. 3462-3470.
- 8 J.A. Collins, A. Rudenski, J. Gibson, L. Howard, R. O'Driscoll, Relating oxygen partial pressure, saturation and content: the haemoglobin-oxygen dissociation curve, *Breathe* 11 (3) (2015), pp. 194-201.
- 9 Q. Gu, T. Joglekar, C. Bieberich, R. Ma, L. Zhu, Nanoparticle redistribution in PC3 tumors induced by local heating in magnetic nanoparticle hyperthermia: In vivo experimental study, *ASME Journal of Heat Transfer* 141 (3) (2019), pp. 032402.
- 10 Q. Gu, M.M. Zaw, T. Munuhe, R. Ma, L. Zhu, Nanoparticle re-distribution in tissue-equivalent gels induced by magnetic nanoparticle hyperthermia, *Summer Biomechanics, Bioengineering and Biotransport Conference*, Tucson, AZ, USA (2017) June 21-24<sup>th</sup>. (Paper number SB3C-2017-72).
- 11 M. Singh, R. Ma, L. Zhu, Theoretical evaluation of temperature elevation, thermal damage, transport porosity enhancement, and magnetic nanoparticle migration in tumors during local heating, *Summer Biomechanics, Bioengineering, and Biotransport Conference*, Seven Springs, PA, USA (2019a) June 25-28<sup>th</sup>. (Paper number SB3C-2019-158).
- 12 M. Singh, Q. Gu, R. Ma, L. Zhu, Heating protocol design affected by nanoparticle redistribution and thermal damage model in magnetic nanoparticle hyperthermia for cancer treatment, *ASME J. Heat Transfer* 142 (7) (2020), pp. 072501.
- 13 M. Singh, R. Ma, L. Zhu, Quantitative evaluation of effects of coupled temperature elevation, thermal damage, and enlarged porosity on nanoparticle migration in tumors during magnetic nanoparticle hyperthermia, *International Communications in Heat and Mass Transfer* 126 (2021b), pp. 105393.
- 14 N.L. Gershfeld, M. Murayama, Thermal instability of red blood cell membrane bilayers: Temperature dependence of hemolysis, *Journal of Membrane Biology* 101 (1988), pp. 67-72.
- 15 M. Singh, S. Soni, T. Singh, Pre-operative assessment of ablation margins for variable blood perfusion metrics in a magnetic resonance imaging based complex breast tumour anatomy: Simulation paradigms in thermal therapies, *Journal of Computer Methods and Programs in Biomedicine* 198 (2021a), pp. 105781.
- 16 C.W. Song, M.S. Kang, J.G. Rhee, S.H. Levitt, Effect of hyperthermia on vascular function in normal and neoplastic tissues, *Annals of The New York Academy of Sciences* 335 (1980), pp. 35-47.
- 17 D.S. Rappaport, C.W. Song, Blood flow and intravascular volume of mammary adenocarcinoma 13726A and normal tissues of rat during and following hyperthermia, *International Journal of Radiation Oncology Biology Physics* 9 (4) (1983), pp. 539-547.
- 18 A. Attaluri, S.K. Kandala, M. Wabler, H. Zhou, C. Cornejo, M. Armour, M. Hedayati, Y. Zhang, T.L. DeWesse, C. Herman, R. Ivkov, Magnetic nanoparticle hyperthermia enhances radiation therapy: A study in mouse models of human prostate cancer, *International Journal of Hyperthermia* 31 (4) (2015), pp. 359-374.
- 19 M. Singh, Q. Gu, R. Ma, L. Zhu, Temperature distribution and thermal dosage affected by nanoparticle distribution in tumours during magnetic nanoparticle hyperthermia, *ASME International Conference on Micro/Nanoscale Heat and Mass Transfer* (2019), Paper No: MNHMT 2019-4233, V001T13A002.
- 20 H.H. Pennes, Analysis of tissue and arterial blood temperature in resting forearm, *J. Applied Physiology* 1 (1948), pp. 93-122.

- 21 A. LeBrun, T. Joglekar, C. Bieberich, R. Ma, L. Zhu, Identification of infusion strategy for achieving repeatable nanoparticle distribution and quantification of thermal dosage using micro-CT Hounsfield unit in magnetic nanoparticle hyperthermia, *International Journal of Hyperthermia* 32 (2) (2016a), pp. 132-143.
- 22 G.A. Truskey, F. Yuan, D.F. Katz, *Transport phenomena in biological systems* (Second ed.), Prentice Hall, Upper Saddle River, New Jersey (2009).
- 23 A.W. El-Kareh, S.L. Braunstein, T.W. Secomb, Effect of cell arrangement and interstitial volume fraction on the diffusivity of monoclonal antibodies in tissue, *Biophysical Journal* 64 (1993), pp. 1638-1646.
- 24 A. Zhang, X. Mi, G. Yang, L.X. Xu, Numerical study of thermally targeted liposomal drug delivery in tumor, *ASME Journal of Heat Transfer* 131 (4) (2009), pp. 043209.
- 25 M. Singh, H. Flores, R. Ma, L. Zhu, Extraction of baseline blood perfusion rates in mouse body and implanted PC3 tumor using infrared images and theoretical simulation, *Summer Biomechanics, Bioengineering, and Biotransport Virtual Conference*, Vail, CO, USA (2020c) June 17-20<sup>th</sup>. (Paper No. SB3C-2020-347).
- 26 A. Fasano, D. Hömberg, D. Naumov, On a mathematical model for laser-induced thermotherapy, *Applied Mathematical Modeling* 34 (12) (2010), pp. 3831-3840.
- 27 J.A. Pearce, Improving accuracy in Arrhenius models of cell death: Adding a temperature dependent time delay, *Journal of Biomechanical Engineering* 137 (2015), pp. 121006.
- 28 X. He, S. McGee, J.E. Coad, F. Schmidlin, P.A. Iaizzo, D.J. Swanlund, S. Kluge, E. Rudie, J.C. Bischof, Investigation of the thermal and tissue injury behaviour in microwave thermal therapy using a porcine kidney model, *International Journal of Hyperthermia* 20 (6) 2004, pp. 567-593.
- 29 S. Soni, H. Tyagi, R.A. Taylor, A. Kumar, The influence of tumour blood perfusion variability on thermal damage during nanoparticle-assisted thermal therapy, *International Journal of Hyperthermia* 31 (6) 2015, pp. 615-625.
- 30 J. Lang, B. Erdmann, M. Seebass, Impact of nonlinear heat transfer on temperature control in regional hyperthermia. *IEEE Transaction on Biomedical Engineering* 46 (9) 1999, pp. 1129-38.
- 31 M. Singh, Medical imaging assisted computational bio-heat transfer analysis of magnetic nanoparticles induced hyperthermia for breast cancer, M.S. Thesis Thapar Institute of Engineering and Information Technology, Patiala, Punjab, India (2016). <http://hdl.handle.net/10266/4116>
- 32 M. Singh, R. Ma, L. Zhu, Theoretical evaluation of enhanced nanoparticle delivery to PC3 tumors due to increased hydraulic conductivity or recovered lymphatic function after mild whole body hyperthermia, *Journal of Medical and Biological Engineering and Computing* 59 (2021c), pp. 301-313.
- 33 F.S. Alzahrani, I.A. Abbas, Analytical estimations of temperature in a living tissue generated by laser irradiation using experimental data, *Journal of Thermal Biology* 85 (2019), pp. 102421.
- 34 M.R. Talaei, A. Kabiri, Analytical solution of hyperbolic bioheat equation in spherical coordinates applied in radiofrequency heating, *Journal of Mechanics in Medicine and Biology*, 17 (4) (2017), pp. 1750072.
- 35 A. Kabiri, M.R. Talaei, Theoretical investigation of thermal wave model of microwave ablation applied in prostate Cancer therapy, *Heat and Mass Transfer*, 55 (8) (2019), pp. 2199-2208.
- 36 V. Bernard, E. Staffa, V. Mornstein, A. Bourek, Infrared camera assessment of skin surface temperature – Effect of emissivity. *Physica Medica* 29 (2013), pp. 583-591.

- 37 L. Li, A.M. LeBrun, L.D.T. Topoleski, L. Zhu, Evaluation of sensitivity and accuracy of infrared thermography for melanoma screening, Summer Biomechanics, Bioengineering, and Biotransport Virtual Conference, National Harbor, MD, USA (2016) June 29<sup>th</sup> – July 2<sup>nd</sup> (Paper No. SB<sup>3</sup>C-2016-145).
- 38 M. Singh, Blood perfusion extraction in cancerous lesions using thermal signatures of infrared imaging, inverse heat transfer and anisotropic voxel based mapping of microCT imaging: Modelling and simulation, (2022). <http://dx.doi.org/10.2139/ssrn.4029435>
- 39 S. Thomsen, J. Pearce, Thermal damage and rate processes in biologic tissue, In: A. Welch, M. van Gemert (eds) Optical-thermal response of laser-irradiated tissue, Springer, Dordrecht (2010), pp. 487-549. [https://doi.org/10.1007/978-90-481-8831-4\\_13](https://doi.org/10.1007/978-90-481-8831-4_13)
- 40 D. Van de Sompel, T.Y. Kong, Y. Ventikos, Modelling of experimentally created partial-thickness human skin burns and subsequent therapeutic cooling: A new measure for cooling effectiveness, Medical Engineering and Physics 31 (6) (2009), pp. 624-631.
- 41 F.C. Henriques, Studies of thermal injury V. The predictability and the significance of thermally induced rate processes leading to irreversible epidermal injury", Archives of Pathology 43 (1947), pp. 489-502.
- 42 C.E. Fugitt, A rate process of thermal injury, Armed Forces Special Weapons Project, AFSWP-606 (1955).
- 43 A.M. Stoll, L.C. Greene, Relationship between pain and tissue damage due to thermal radiation, Journal of Applied Physiology 14 (3) (1959), pp. 373-382.
- 44 A. Takata, Development of criterion for skin burns, Aerospace Medicine, 45 (6) (1974), pp. 634-637.
- 45 Y.C. Wu, A modified criterion for predicting thermal injury, National Bureau of Standards, Washington (1982).
- 46 M.N. Rylander, Y. Feng, K. Zimmermann, K. R. Diller, Measurement and mathematical modelling of thermally induced injury and heat shock protein expression kinetics in normal and cancerous prostate cells, International Journal of Hyperthermia 26 (8) (2010), pp. 748-764.
- 47 Y. Feng, J.T. Oden, M.N. Rylander, A two-state cell damage model under hyperthermic conditions: Theory and in vitro experiments, Journal of Biomechanical Engineering 130 (4) (2008), pp. 041016.
- 48 J. A. Pearce 2015, Improving accuracy in Arrhenius models of cell death: Adding a temperature dependent time delay, Journal of Biomechanical Engineering 137 (12) (2015), pp. 121006.
- 49 A. Attaluri, R. Ma, Y. Qiu, W. Li, L. Zhu, Nanoparticle distribution and temperature elevations in prostatic tumours in mice during magnetic nanoparticle hyperthermia, International Journal of Hyperthermia 27 (5) (2011), pp. 491-502.
- 50 R. Xu, H. Yu, Y. Zhang, M. Ma, Z. Chen, C. Wang, G. Teng, J. Ma, X. Sun, N. Gu, Three-dimensional model for determining inhomogeneous thermal dosage in a liver tumor during arterial embolization hyperthermia incorporating magnetic nanoparticles, IEEE Transactions on Magnetics 45(8) (2009), pp. 3085-3091.
- 51 M. Johannsen, A. Jordan, R. Scholz, M. Koch, M. Lein, S. Deger, J. Roigas, K. Jung, S. Loening, Evaluation of magnetic fluid hyperthermia in a standard rat model of prostate cancer, Journal of Endourology 18(5) (2004), pp. 495-500.
- 52 A. Jordan, R. Scholz, P. Wust, H. Föhling, J. Krause, W. Wlodarczyk, B. Sander, Th. Vogl, R. Felix, Effects of magnetic fluid hyperthermia (MFH) on C3H mammary carcinoma *in vivo*, International Journal of Hyperthermia 13 (1997), pp. 587-605.

- 53 A. Miaskowski, M. Subramanian, Numerical model for magnetic fluid hyperthermia in a realistic breast phantom: calorimetric calibration and treatment planning, *International Journal of Molecular Sciences* 20 (2019), pp. 4644.
- 54 M. Singh, M. Dalal, G.S. Sodhi, Estimation of clinical size of breast tumour lesions using contrast enhanced magnetic resonance imaging: Delineation of tumour boundaries, *Summer Biomechanics, Bioengineering, and Biotransport Virtual Conference*, Vail, CO, USA (2021d) June 14-18<sup>th</sup>. (Paper No. SB3C-2021-355). <https://doi.org/10.31224/osf.io/enx4r>



**Manpreet Singh** is currently a Ph.D. research scholar in the Department of Mechanical Engineering at *University of Maryland Baltimore County, Baltimore, Maryland, USA*. He is presently working on NSF funded project title “*Mild Hyperthermia to enhance delivery of therapeutic nanocarriers in tumors: imaging, in vivo study, and simulation*” and have also possess internship experience at “*Maryland Proton Treatment Center*”, *University of Maryland School of Medicine*. His research interests include Image based computational modelling approach to plan, develop and optimize protocols in clinical hyperthermia, hypothermia therapies. Singh is presently developing integrated computationally-predictive models based on in-vivo laboratory experiments on PC3 tumors to understand the interplay between different nanoparticle-mediated heat and mass transport mechanisms. His research explains the correlation among blood perfusion, permeability, porosity, interstitial fluid pressure, diffusion, accumulation,

retention, penetration, and vascular tortuosity affected by heating and providing means to extrapolate the in-vivo results from mouse models to clinical applications. In 2017, he had worked with company *Capillary Biomedical Inc., California* on a NIH funded project in association with *Rowan University, New Jersey* and *Thomas Jefferson University, Pennsylvania* to design novel multi-perforated infusion catheters for type-1 diabetes patients.